ACS APPLIED MATERIALS & INTERFACES

www.acsami.org
Research Article

Photoinduced Charge Injection from Shallow Point Defects in Diamond into Water

Kang Xu, Daniela Pagliero, Gabriel I. López-Morales, Johannes Flick, Abraham Wolcott, and Carlos A. Meriles*

Cite This: ACS Appl. Mater. Interfaces 2024, 16, 37226−37233
Read Online

ABSTRACT: Thanks to its low or negative surface electron affinity and chemical inertness, diamond is attracting broad attention as a source material of solvated electrons produced by optical excitation of the solid−liquid interface. Unfortunately, its wide bandgap typically imposes the use of wavelengths in the ultraviolet range, hence complicating practical applications. Here, we probe the photocurrent response of water surrounded by single-crystal diamond surfaces engineered to host shallow nitrogen-vacancy (NV) centers. We observe clear signatures of diamond-induced photocurrent generation throughout the visible range and for wavelengths reaching up to 594 nm. Experiments as a function of laser power suggest that NV centers and other coexisting defects—likely in the form of surface traps—contribute to carrier injection, though we find that NVs dominate the system response in the limit of high illumination intensities. Given our growing understanding of near-surface NV centers and adjacent point defects, these results open new perspectives in the application of diamond−liquid interfaces to photocarrier-initiated chemical and spin processes in fluids.

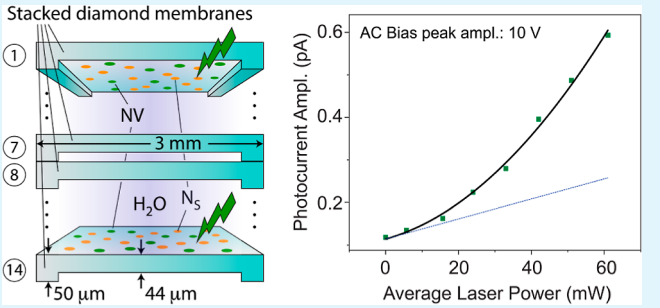

KEYWORDS: *diamond, NV centers, shallow traps, solvated carriers, photocurrent*

INTRODUCTION

Injection, migration, and collection of photogenerated charges across solid−fluid interfaces are central to applications in electrochemistry,[1,2] photocatalysis,[3] and biology.[4] From a growing palette of source materials,[5,6] diamond is drawing broad interest because it is chemically inert and its low or negative surface electron affinity facilitates the formation of solvated charges.[7,8] Electron injection from diamond into aqueous environments is attracting special attention given the electron's capacity to trigger reactions otherwise difficult to induce catalytically; examples include the reduction of dissolved N_2 to NH_3 or CO_2 into CO.[7,9,10] Carrier injection from diamond should also prove relevant to the study of confined fluidic environments, for example, to help understand ion transport in biomembranes[11] or investigate memristic responses in nanofluidic channels.[12] related lines, the ability to optically inject carriers previously spin polarized via optical and/or microwave manipulation could open new routes toward dynamic nuclear polarization in fluids[13,14] or in the exploration of spin-selective transport across liquid−solid interfaces.[15] We note that although other materials with favorable electron affinity are known,[16,17] most react with water, which further singles out diamond as a preferred platform.

In the absence of midbandgap states, free carrier excitation requires the use of ultraviolet (UV) illumination with a wavelength of 227 nm or shorter. Given the impracticalities of UV light, different strategies are being explored to reduce the photon energy to the visible range; these include functionalization with dye molecules,[18] plasmonic coupling via embedded metal nanoparticles,[19] surface nanostructuring,[20] and the use of dopants such as boron, nitrogen, or phosphorus.[21] Experiments using ultrafast transient absorption spectroscopy demonstrated the injection of solvated electrons into water from surface-terminated detonation nanodiamond under 400 nm laser excitation.[22] Additionally, emission spectroscopy experiments on thin polycrystalline diamond films subject to light excitation of variable wavelength have shown electron injection into vacuum throughout the near-UV and visible range, from 340 to 550 nm.[23]

Here, we implement photocurrent measurements to probe carrier injection into ultrapure water from single-crystal,

Received: April 17, 2024
Revised: June 18, 2024
Accepted: June 20, 2024
Published: July 8, 2024

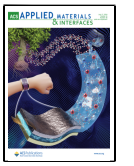

https://doi.org/10.1021/acsami.4c06298
ACS Appl. Mater. Interfaces 2024, 16, 37226−37233

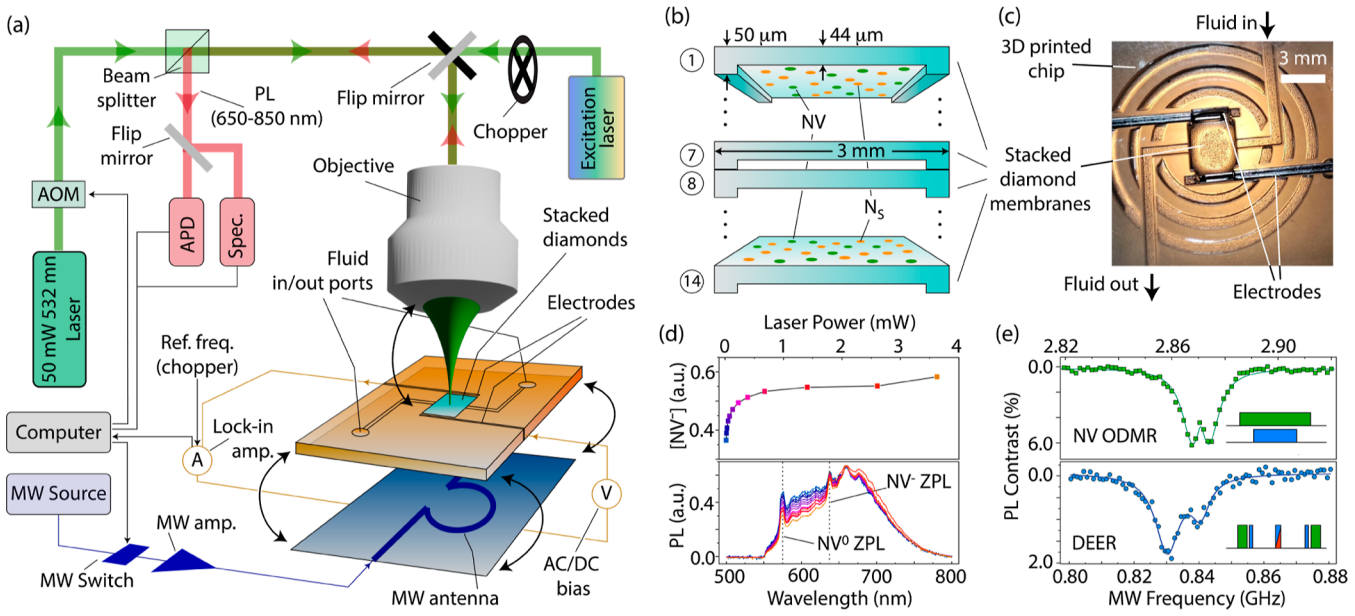

Figure 1. Optofluidic setup. (a) Schematic of the experimental setup. We use a microfluidic device to circulate a fluid through the 6 μm-tall spacings in a stack of fourteen 44-μm-thick, 3 × 3 mm^2 diamond membranes hosting 5 nm-deep NVs on either side. The system can be configured to operate as a confocal microscope or for photocurrent measurements. In this latter case, we apply a bias AC or DC voltage with the aid of two lateral gold-coated electrodes in contact with the fluid and measure the photocurrent using a lock-in amplifier. (b) Side-view schematics of the diamond membrane stack. (c) Optical image of the microfluidic chip; adhesive in the circular trenches around the diamond chamber holds a thin glass coverslip serving as the upper seal. (d) Fluorescence spectroscopy of a representative diamond membrane for optical power growing from 12 μW (blue) to 3.6 mW (orange). The upper plot shows the fractional NV$^-$ population as extracted from fits to the optical spectra. (e) Continuous-wave optically detected magnetic resonance (ODMR) of the NVs in one of the membranes and NV-detected DEER spectrum of coexisting paramagnetic impurities (upper and lower plots, respectively). Solid traces indicate fits of two Lorentzian curves. Green blocks indicate 532 nm laser pulses while blue and red blocks, respectively, represent MW pulses resonant with the NVs and coexisting paramagnetic centers, see Methods. In (d,e), we configure the microscope in confocal mode, i.e., we excite and collect luminescence from an ∼1 μm^2 area in one of the NV layers of a single, representative diamond membrane. AOM: acousto-optic modulator. APD: avalanche photodetector. Amp: amplifier. PL: photoluminescence. Spec.: PL spectrometer. ZPL: zero-phonon line. Ref. freq: reference frequency from the chopper.

oxygen-terminated diamond engineered to feature optimal nitrogen-vacancy (NV) concentration from annealing-induced conversion of shallow-implanted nitrogen. Already exploited as nanoscale sensors,[24−26] NV centers promise opportunities as a source of solvated carriers because visible light induces a cycle of charge-state conversion,[27] from negatively charged (NV$^-$) to neutral (NV^0) and back, respectively, resulting in the generation of free electrons and holes.[28,29] With the help of a microfluidics chip tailored to yield a large contact area between water and single crystal diamond, we demonstrate steady-state photocurrent generation in water under visible light, which we attribute to a subtle interplay between contributions from NV centers—dominant at higher laser intensities and photo-activated surface traps.

Experimental Approach and Diamond Characteristics. Figure 1a lays out our setup: the key piece in our experiments is a microfluidic device designed to host a stack of fourteen 44-μm-thick membranes made from electronic grade, single-crystal diamond. ^{14}N implantation on both sides of each membrane followed by thermal annealing yield ∼5 nm-deep NV layers with a concentration of 3 × 10^{11} cm^{-2}. From the implantation conditions, we estimate a nitrogen content of 1 × 10^{13} cm^{-2}, which corresponds to an NV formation efficiency of 3%, characteristic for near-surface centers[30] (see Methods). Exposure to acid mixtures prior to usage ensures predominantly oxygen-terminated surfaces[31] though the coverage is likely chemically and spatially heterogeneous with varying content of carbonyl and hydroxyl groups; remarkably, the surface electron affinity may remain negative due to persistent C−H bonds.[8,31−33] Throughout all charge injection experiments, we slowly flow water through the 6 μm openings between adjacent membranes as well as the 30 μm gap space between the electrodes and diamonds (Figure 1b,c). We use collimated optical excitation of variable wavelength to homogeneously illuminate a 2 mm-diameter area of the membranes and measure the resulting photocurrent with the help of a lock-in amplifier referenced to an optical chopper modulating the excitation beam at 2 kHz.

The use of engineered single-crystal diamond leads to high-quality surfaces, which, in turn, allows us to implement optical and spin characterization protocols otherwise difficult to replicate. We selectively probe the fluorescence stemming from individual NV layers in the stack with our microscope configured in "confocal" mode upon a simple reconfiguration of the excitation beam path (Figure 1a). For illustration purposes, Figure 1d shows representative photoluminescence (PL) spectra from an ∼1 μm^2 section in one of the membranes for different laser powers. A decomposition into negative and neutral contributions yields an intensity-dependent NV$^-$ fractional population evolving from ∼30% at the lowest laser powers to saturate at ∼60%, below the 75% limit characteristic of bulk NVs under 532 nm illumination.[27] This lower-than-normal NV$^-$ fraction is indicative of partial NV$^-$ ionization in the dark, likely due to tunneling of the excess electron to adjacent traps[34,35] and/or capture of itinerant near-surface holes.[36]

https://doi.org/10.1021/acsami.4c06298
ACS Appl. Mater. Interfaces 2024, 16, 37226−37233

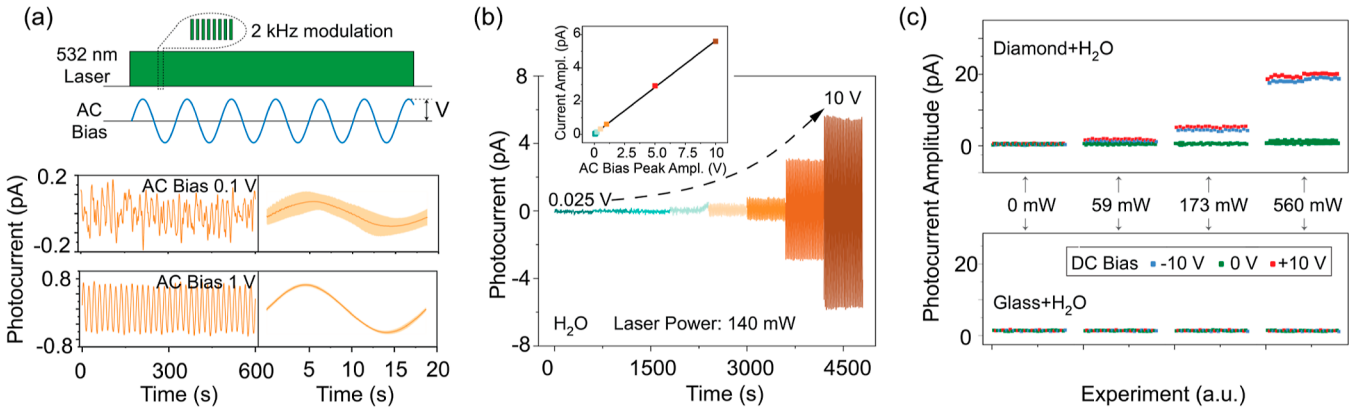

Figure 2. Detection of photocurrent in water. (a) Experimental protocol (top) and example photocurrent signals (bottom left) for pure H_2O; the AC bias frequency is 53 mHz, the lock-in integration constant is 1 s, and the laser power is 140 mW. The lower right plots are one-cycle averages, here used for error determination. (b) Observed photocurrent temporal signals from H_2O for varying AC voltage bias; the 532 nm laser power is 140 mW. The upper inset shows the photocurrent peak amplitude vs the AC bias peak amplitude as derived from the main plot. (c) H_2O photocurrent signal amplitudes with and without applied DC bias for varying laser intensities when in contact with a diamond or a glass stack of membranes (left and right plots, respectively). In all experiments, the beam illuminates a 2 mm-diameter spot extending uniformly across all membranes.

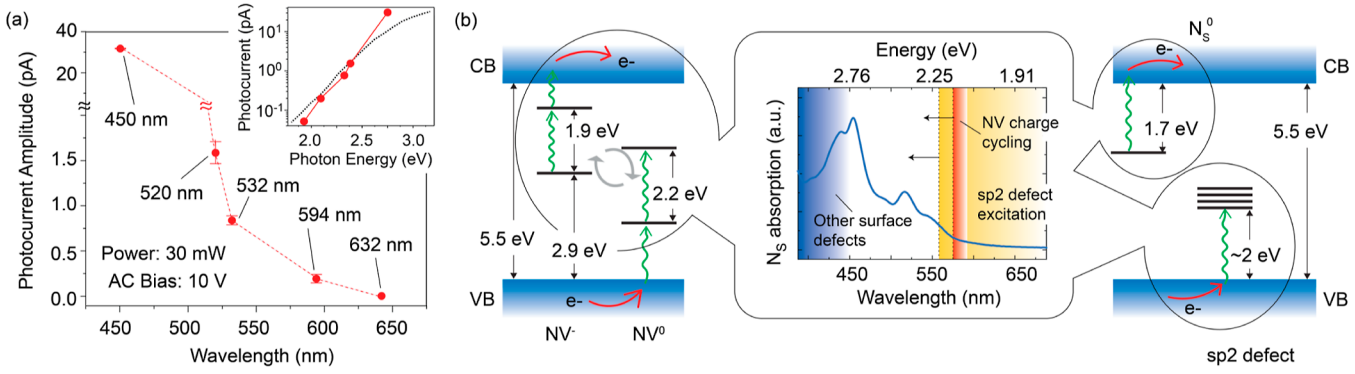

Figure 3. Photocurrent response at varying wavelengths. (a) Photocurrent amplitude as a function of the excitation wavelength. The inset shows the same data set but in logarithmic scale vs photon energy; the dashed black line reproduces the data set in ref 51. In all cases, the AC voltage bias is 10 V and the excitation laser power is 30 mW for an illuminated area of ~2 mm^2; all other conditions as in Figure 2. (b) Main plot, calculated N_S^0 ionization cross section vs wavelength as derived from density functional theory (DFT) (solid trace). The red band indicates the range where two-photon NV charge cycling activates, see ref 29; orange and blue areas, respectively, indicate activation bands of single-photon electron injection into unoccupied states in primal sp^2 defects and other surface defects as derived from refs 10 and 52, respectively. (Left inset) schematics of NV two-photon ionization and recombination, left- and right-hand side diagrams, respectively. (Right inset) single-photon processes corresponding to N_S^0 photoionization and electron injection into surface traps (top left and bottom right diagrams, respectively). CB: conduction band; VB: valence band.

Observations of ODMR—possible in NV^- thanks to its spin-dependent photon emission[37,38]—provide additional clues on the surface characteristics. The upper plot in Figure 1e shows the ODMR spectrum obtained upon a microwave (MW) sweep across the NV^- zero-field resonance.[39] We attain an optical spin contrast of ~6%, lower than the 30% optimum but better than typically observed in similarly shallow NV ensembles.[40] The measured line width (~8 MHz) is moderate, especially if we consider the underlying ^{14}N hyperfine broadening and the characteristically large strain- and electric-field-induced heterogeneity of the NV^- crystal field near the surface. On the other hand, the relatively short spin–echo lifetime (~2 μs, not shown) is characteristic of NVs subjected to magnetic and electric noise near the surface.[41−43]

We interrogate coexisting paramagnetic centers via NV-detected double electron–electron resonance (DEER) experiments (low inset in Figure 1e). The DEER spectrum features two dips of comparable amplitude, indicative of multiple classes of spin-active defects.[44−46] Interestingly, we find no characteristic PL dips at the hyperfine-shifted frequencies of neutral substitutional nitrogen[46] (N_S^0) suggesting the loss of the donor electron and thus the formation of N_S^+, a spin-less charge state. Likely the result of incomplete surface oxidation,[8] we interpret these observations as indicative of a positive band bending strong enough to deplete N_S^0 (a shallower donor) but only partially affecting NV^-. We return to these important considerations in the following section.

Photocurrent Measurements in Water. Figure 2a introduces our experimental protocol comprising laser excitation and an alternating (AC) voltage bias between the electrodes, here introduced to minimize space charge fields[47] (see Methods). Because the AC frequency (in the mHz range) is much slower than the laser modulation rate (2 kHz) and lock-in inverse integration time (typically, 1 s^{-1}), each point in the photocurrent plot can be seen as an "instantaneous" measurement under a varying direct (DC) bias field. The lower

https://doi.org/10.1021/acsami.4c06298
ACS Appl. Mater. Interfaces 2024, 16, 37226−37233

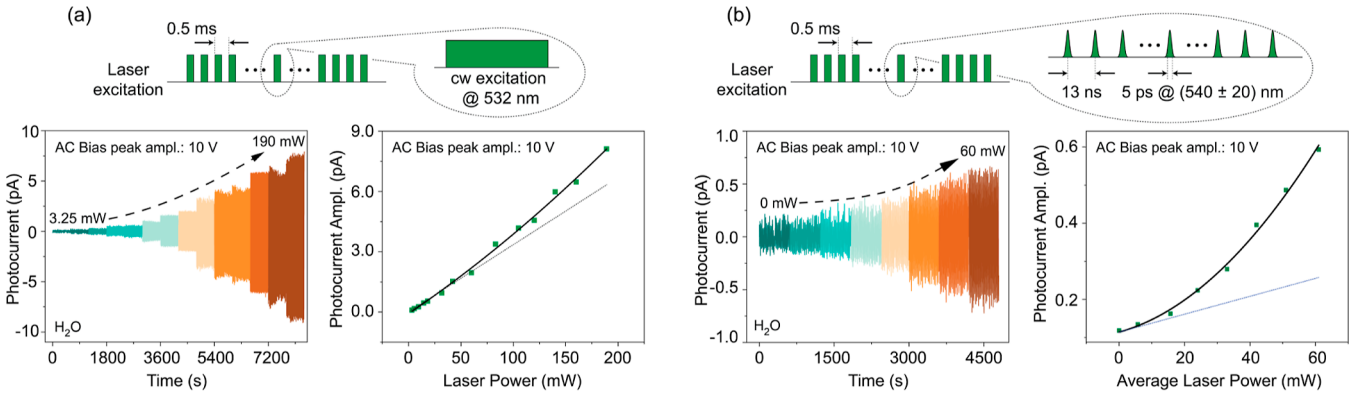

Figure 4. Photocurrent response at varying laser power. (a) We reproduce the protocol in Figure 2a, except that this time we gradually change the 532 nm laser power for a fixed AC bias amplitude (10 V). The lower right plot shows the photocurrent amplitude as extracted from the raw data (left plot). The solid line is a quadratic fit with a linear component plotted separately as a dashed line. (b) Same as in (a) but for light excitation from a supercontinuum laser producing a 78 MHz train of 5 ps-long pulses with a wavelength dispersion of 40 nm centered at 540 nm. Unless otherwise stated, working conditions are those in Figure 2.

plots in Figure 2a display representative data sets under 532 nm excitation and AC bias of different maximum amplitude; using one-cycle averages to quantify the error (bottom right plots), we benchmark the photocurrent sensitivity of our setup at about 0.6 pA $Hz^{-1/2}$.

The use of a sinusoidal shape to fit our observations necessarily hinges on a linear relation between the photocurrent and applied AC bias, a condition we verify via measurements under varying AC field amplitudes (Figure 2b); the proportionality we observe mirrors the Ohmic response we find in our water-filled chip in the absence of optical excitation. Importantly, we measure zero photocurrent—even at the highest possible laser intensities—if we replace the membranes by an equal number of glass slides arranged in identical geometry, which simultaneously demonstrates the key role of the diamond−water interface as well as our ability to separate the photogenerated current from background (i.e., light-insensitive) contributions (Figure 2c).

Although the system at hand has been explicitly designed to make NVs abundant, the nature of the point defect serving as the carrier source is difficult to disambiguate as ion implantation leads to concomitant point defects potentially susceptible to charge-state changes under optical illumination. An initial route to deconvolving contributions from NVs and these coexisting sources involves the characterization of photocurrent under illumination of variable wavelength. We capture these experiments in Figure 3a: in the absence of a light source with the required tunability and output power, we adapt the setup in Figure 1a to accommodate continuous wave (cw) lasers at discrete wavelengths throughout the visible range. Relative to our observations at 532 nm (Figure 2), we find a quick jump of the photocurrent amplitude at shorter wavelengths, with an ∼30-fold increase at 450 nm; as the wavelength grows, however, we measure a monotonic decrease to attain virtually no response at 632 nm (and beyond).

While the above findings are insufficient to expose a specific point defect as the dominant source, the observed spectral dependence does contain some important clues. For example, the trend at longer wavelengths (i.e., 594 and 632 nm) is not inconsistent with that expected for NVs because the two-step, one-photon processes driving NV charge cycling at 532 and 520 nm get suppressed above 575 nm (where the photon energy is insufficient to excite NV^0). Phonon-assisted recombination at longer wavelengths makes this transition gradual,[27,48] hence implying that an NV-dominated photocurrent would arguably fall off smoothly, as observed. As a matter of fact, this wavelength dependence qualitatively reproduces that observed for NV ensembles in bulk diamond[49] (inset in Figure 3a).

Unfortunately, this trend is not unique and hence insufficient to separate NV centers from other potential charge sources. Among them, substitutional nitrogen (N_S) is a natural candidate: despite its 1.7 eV (i.e., 730 nm) ionization threshold, large structural reconfigurations[50,51] required for $N_S^0 \rightarrow N_S^+$ conversion make optical excitation inefficient for photon energies below ∼2.1 eV, hence pushing free carrier activation to wavelengths below ∼590 nm. Since the observed photocurrent should reflect the N_S^0 absorption cross section—explicitly calculated in Figure 3b via DFT, see Methods—one would also expect in this case a gradual signal change in the 500−650 nm range, not too different from our experimental results.

Assigning the photocurrent spectral response to $N_S^0 \rightarrow N_S^+$ conversion, however, seems unwarranted, particularly given the absence of N_S^0 DEER signal discussed above. Furthermore, the photocurrent response at 450 nm is about 30-fold larger than that observed at 532 nm and hence disproportionally big for a process solely dominated by nitrogen defects (see Figure 3b as a reference). The origin of this steep change at shorter wavelengths is presently unclear, but we hypothesize that it stems from charge injection produced by excitation of unoccupied surface states.[8,22] These take varying forms depending on the fluid in contact with the crystal and surface termination protocol, but they are known to activate under blue excitation and are generally abundant in chemically oxidized diamond surfaces.[8] Similarly, the response above ∼520 nm could be due to primal sp^2 surface defects, recently shown to serve as electron traps in the 1.5−2.2 eV range above the valence band maximum.[52] Upward band bending takes place near the surface as these electronic traps (partially) fill out in nitrogen-doped diamond,[53] thus explaining the depletion of N_S^0 and the lower-than-normal concentration of NV^-. Furthermore, electron capture renders these defects paramagnetic, thus providing a rationale for the observed DEER signal; note that in the absence of spin-active nuclei—other than 1%-abundant ^{13}C—magnetic resonance signals

https://doi.org/10.1021/acsami.4c06298
ACS Appl. Mater. Interfaces 2024, 16, 37226−37233

should not display hyperfine satellites, consistent with our observations in Figure 1e.

In a scenario where NVs coexist with surface traps, one route to separating individual photocurrent contributions is to exploit their distinct charge-state responses to light, respectively, governed by two- or single-photon processes, and thus leading to quadratic or linear signal changes under varying illumination intensity. Figure 4a extends the observations in Figure 2 to examine the photocurrent signal for variable laser powers. We limit these experiments to 532 nm excitation, chosen to ensure significant NV charge cycling while restricting the type of surface defects to primal sp^2 traps (featuring unoccupied levels accessible to this wavelength[52]). Analogous to photocurrent measurements in bulk-type 1b diamond—often dominated by single photon charge injection processes[54]—the response we observe is predominantly linear, even though a quadratic correction is clearly necessary to attain a good fit. Given the one-photon nature of electronic injection in sp^2 defects, our results point to these surface traps, not the NVs, as the dominant carrier source in these experiments. Interestingly, photoelectrically detected magnetic resonance[54,55] (PDMR) experiments—implemented herein through the combined use of our optical excitation and MW capabilities—yield no observable signal at the characteristic NV^- crystal field frequency, which indirectly supports the above conclusion.

The small but discernible quadratic contribution we extract from Figure 4a, however, suggests that NV centers can indeed play a significant role if the illumination intensity is sufficiently high. We validate this idea in Figure 4b where, rather than cw excitation, we make use of a supercontinuum laser producing a train of picosecond-long pulses at a repetition rate of 78 MHz (see Methods). To bring the average power to a range comparable to that attained with the cw light source, we set a 40 nm spectral window centered at 540 nm. Remarkably, we find that increasing the (average) laser power leads to a predominantly parabolic signal growth, indicative of NV-dominated photocurrent. This change can be rationalized as a manifestation of the quadratic power dependence inherent to two-photon ionization/recombination processes and hence the augmented impact of picosecond pulses on the NV charge-cycling dynamics. As an important side note, attempts to observe a PDMR signal from NVs exposed to pulsed illumination yielded inconclusive results. In this case, we attribute the lack of a clear spectral signature to the combination of a weak photocurrent signal (in the fA range under present conditions) and the rather modest PDMR contrast (typically 3−10% in ensembles). This limitation could be circumvented in future experiments through the use of higher power femtosecond lasers operating in the visible range.

CONCLUSIONS AND OUTLOOK

In summary, we leveraged diamond engineering and microfluidics to investigate photoactivated carrier transfer into water. Unlike most prior work—typically relying on boron-doped, hydrogen-terminated diamond—here, we focused on oxygen-terminated, electronic-grade single crystals engineered to host near-surface NV centers; in these samples, chemical oxidation counters band bending and hence maintains a significant fraction of NVs in the negatively charged state. We detect photocurrent throughout the visible range, although the amplitude decreases with longer wavelengths to become negligible above 600 nm. Combined with ODMR and photocurrent measurements under varying laser power and wavelength, our observations expose photocurrent contributions from NV centers and other coexisting point defects, most likely associated with surface acceptors. This latter group—probably formed by primal sp^2 defects or dangling bonds (or both)—dominates photocurrent injection under weaker green illumination; pulsed excitation, on the other hand, efficiently activates two-photon processes, ultimately making the NV contribution prevalent.

Future work should identify the conditions for optimal carrier injection without compromising, the concentration of NV^-. Similarly, rendering NVs the main source of photogenerated carriers will rely on new strategies able to improve the NV formation efficiency during the anneal[56] and/or the use of pulsed excitation with time-averaged power higher than that possible here. Additional theoretical and experimental work will also be necessary to better understand the mechanisms responsible for replenishing carriers in the color center ensemble, mitigate the formation of space charge fields, best assess the role of heterogeneity in surface termination, and determine fractional contributions to the photocurrent from injected electrons and holes.

The use of single-crystalline diamond hosting shallow, long-spin-coherence paramagnetic centers opens intriguing opportunities for the investigation of solvated-carrier-initiated chemical reactions. Of particular interest are experiments in nanoscale confined media—produced, e.g., with the help of patterned two-dimensional materials[57]—where the proximity to shallow NV^- could be simultaneously exploited to implement optical−magnetic-resonance-based sensing approaches.[58] These ideas could prove especially fruitful in the investigation of ionic transport in nanofluidic channels and their application to fluidic neuromorphic computing.[12] While the focus here centered on liquids, electron injection into vacuum seems similarly possible[23] and could be leveraged to develop new forms of single-NV-based electron microscopies, an interesting feature being the ability to monitor the number of photogenerated carriers via, e.g., single-shot NV charge-state readout.[59,60]

Another attractive possibility entails the implementation of alternate dynamic nuclear polarization strategies via direct injection of spin-polarized carriers into the fluid or through their capture by surface defects in direct interfacial contact. In the case of the NV, the generation of spin-polarized electrons could be accomplished by proper optical initialization preceding ionization;[61] similarly, double resonance schemes could be adapted to transfer spin polarization to surface paramagnetic centers,[62] followed by targeted optical ionization. Mirroring hyperpolarization techniques such as SPINOE,[63] injection of spin-polarized carriers may open new pathways for the transfer of polarization to a fluid,[13] thus far inefficient due to losses introduced by surface paramagnetic impurities during spin diffusion[14] (a comparatively slow process). Combined with photocurrent measurements, this class of experiments should also prove relevant in the investigation of spin-dependent charge transfer across solid−liquid interfaces, demonstrated recently though requiring strong spin-polarizing fields.[15]

METHODS

Sample Characteristics. We utilize 14 customized [100] electronic-grade diamond membranes provided by Qnami AG. Each membrane has dimensions $3 \times 3 \times 0.05$ mm^3 and features a 6 μm-

https://doi.org/10.1021/acsami.4c06298
ACS Appl. Mater. Interfaces 2024, 16, 37226−37233

deep, 2.5 mm-wide, 3 mm-long trench produced via reactive ion etching on one of its surfaces. For a stacked set of membranes, these trenches create 6 μm-wide openings effectively serving as channels for liquid flow (see Figure 1). ^{14}N ion implantation with an energy of 2.5 keV and a dose of 1×10^{13} ions/cm^2 leads to a 5 nm-deep layer of nitrogen spread over an ∼2 nm range as derived from SRIM simulations.[64] To induce NV center formation, known annealing protocols were used,[65] except that the end temperature was 1000 C instead of 800 C. Following annealing, a triacid mixture was used for cleaning and oxygen terminating the diamond surface.

Microfluidic Device. The membranes were placed within a custom-built 3D-printed microfluidic cell, and sealed with a thin glass layer so as to enable laser excitation. The microfluidic cell was equipped with two ports for the flow of aqueous solutions past the diamond membrane's channels and a pair of planar, gold-coated electrodes proximal to the membrane's edge. These electrodes connect to a voltage source and a lock-in amplifier operating as an ammeter (Figure 1c). An automated syringe pump gives us precise control over the liquid flow rate, which we keep at the minimum required to mitigate the formation of space charge fields.

Experimental Setup. Our system can be alternatively configured for photocurrent experiments or for optical characterization of the NV ensemble. In photocurrent measurement mode, we illuminate the diamond stack with a 1 W laser collimated over an $\sim 2 \times 2$ mm^2 area, which remains approximately uniform throughout the membrane stack. The photocurrent from the electrode is measured by a lock-in amplifier, with the current signal locked to the chopper frequency. A set of cw diode lasers, each operating at a different color allows us to investigate the photocurrent response at different illumination wavelengths; for pulsed excitation, we resort to a supercontinuum laser (*NKT*) whose wavelength range we control with a set of integrated filters; the pulsed duration is 5 ps and the repetition rate is 78 MHz.

A flip mirror switches the system to a confocal microscope. In this mode, we choose a target membrane from the stack and steer the photoluminescence to an avalanche photodetector or to a spectrometer, depending on the end application; in this operating mode, we collect fluorescence from an ∼5 μm-long focal volume, and the illuminated area is ∼1 μm^2. Continuous-wave ODMR under aqueous conditions uses the MW generated by an omega-shaped antenna patterned on a PCB board. We use a pulse controller as well as optical and MW switches to program arbitrary time-resolved ODMR protocols including the Hahn-echo and DEER sequences.

Magnetic Resonance. We characterize surface NVs and coexisting paramagnetic centers with the help of ODMR techniques. Continuous-wave ODMR (upper plot in Figure 1e) records the NV fluorescence resulting from 532 nm, 0.6 mW laser illumination in the presence of cw MW excitation of variable frequency (respectively, green and blue blocks in the figure inset). The DEER protocol (lower plot in Figure 1e) comprises initialization and detection laser pulses (532 nm, 0.6 mW, green blocks) enclosing a fixed-duration Hahn echo sequence resonant with the NV $^3A_2$ $|m_S = 0\rangle \leftrightarrow |m_S = -1\rangle$ transition (blue blocks in the inset). The DEER spectrum emerges as one varies the frequency of a second MW π-pulse (nearly) overlapping in time with the Hahn-echo inversion pulse[46] (red block in the inset).

Density Functional Theory. To calculate the N_S^0 absorption cross section, we use the PAW method[66] with Perdew–Burke–Ernzerhoff (PBE)[67] and range-separated Heyd–Scuseria–Ernzerhoff (HSE06)[68] functionals to account for electronic exchange–correlation interactions during atomic relaxations and self-consistent (SCF) calculations, respectively. For the plane-wave basis, we use a cutoff of 370 eV yielding well-converged results.[49,69,70] We attain equilibrium defect structures by embedding the nitrogen impurity in a $4 \times 4 \times 4$ (512-atom) pristine diamond supercell and relaxing the atoms until net forces are below 10^{-3} eV/Å. During SCF calculations, electronic loops converge to energy differences below 10^{-8} eV. We sample the Brillouin zone only at the Γ-point in all supercell calculations. One exception, though, is when calculating the N_S^0 wave function derivatives (used for obtaining transition dipole moments in the momentum representation), in which case, we employ a $6 \times 6 \times 6$ *k*-point Γ-centered sampling mesh, enough to attain good convergence. We obtain the ionization cross section following the scheme described in ref 49. In particular, we correct the N_S^0 ionization response with the Franck–Condon shift to account for the large atomic reconfiguration at N_S^0 electronic ionization threshold.[50,51]

AUTHOR INFORMATION

Corresponding Author

Carlos A. Meriles − *Department of Physics, CUNY-City College of New York, New York, New York 10031, United States; CUNY-The Graduate Center, New York, New York 10016, United States;* orcid.org/0000-0003-2197-1474; Email: cmeriles@ccny.cuny.edu

Authors

Kang Xu − *Department of Physics, CUNY-City College of New York, New York, New York 10031, United States*

Daniela Pagliero − *Department of Physics, CUNY-City College of New York, New York, New York 10031, United States*

Gabriel I. López-Morales − *Department of Physics, CUNY-City College of New York, New York, New York 10031, United States*

Johannes Flick − *Department of Physics, CUNY-City College of New York, New York, New York 10031, United States; CUNY-The Graduate Center, New York, New York 10016, United States; Center for Computational Quantum Physics, Flatiron Institute, New York, New York 10010, United States*

Abraham Wolcott − *Department of Physics, CUNY-City College of New York, New York, New York 10031, United States; Department of Chemistry, San José State University, San José, California 95192, United States;* orcid.org/0000-0002-4025-3040

Complete contact information is available at: https://pubs.acs.org/10.1021/acsami.4c06298

Author Contributions

K.X., D.P., A.W., and C.A.M. conceived the experiments. K.X., A.W., and D.P. conducted the experiments. G.I.L.M and J.F. carried out the DFT calculations. C.A.M. supervised the project and wrote the manuscript with input from all authors.

Notes

The authors declare no competing financial interest.

ACKNOWLEDGMENTS

We thank Alexander Pines for early discussion and help procuring the diamond membranes. We are indebted to Artur Lozovoi for valuable assistance with the experimental setup. We also acknowledge Nicolas Giovambattista, Gustavo Lopez, Alastair Stacey, Jonathan Owen, and Nathalie de Leon for helpful insights. K.X. and C.A.M acknowledge support from the National Science Foundation through NSF-2223461. D.P. acknowledges funding from the National Science Foundation via grant NSF-2203904. A.W. acknowledges funding from the National Science Foundation via grant NSF-2112550. G.I.L.M. acknowledges support from the National Science Foundation via fellowship NSF-2208863. All authors acknowledge access to the facilities and research infrastructure of the NSF CREST IDEALS, grant no. NSF-2112550. The Flatiron Institute is a division of the Simons Foundation.

REFERENCES

(1) Yang, X.; Wolcott, A.; Wang, G.; Sobo, A.; Fitzmorris, R. C.; Qian, F.; Zhang, J. Z.; Li, Y. Nitrogen-doped ZnO nanowire arrays for photoelectrochemical water splitting. *Nano Lett.* **2009**, *9*, 2331−2336.

(2) Yan, Y.; Crisp, R. W.; Gu, J.; Chernomordik, B. D.; Pach, G. F.; Marshall, A. R.; Turner, J. A.; Beard, M. C. Multiple exciton generation for photoelectrochemical hydrogen evolution reactions with quantum yields exceeding 100%. *Nat. Energy* **2017**, *2*, 17052.

(3) Fang, S.; Rahaman, M.; Bharti, J.; Reisner, E.; Robert, M.; Ozin, G. A.; Hu, Y. H. Photocatalytic CO_2 reduction. *Nat. Rev. Methods Primers* **2023**, *3*, 61.

(4) Siefermann, K. R.; Abel, B. The hydrated electron: A seemingly familiar chemical and biological transient. *Angew. Chem., Int.* **2011**, *50*, 5264−5272.

(5) Hoffmann, M. R.; Martin, S. T.; Choi, W.; Bahnemann, D. W. Environmental applications of semiconductor photocatalysis. *Chem. Rev.* **1995**, *95*, 69−96.

(6) Henderson, M. A. A surface science perspective on TiO_2 photocatalysis. *Surf. Sci. Rep.* **2011**, *66*, 185−297.

(7) Zhu, D.; Zhang, L. H.; Ruther, R. E.; Hamers, R. J. Photo-illuminated diamond as a solid-state source of solvated electrons in water for nitrogen reduction. *Nat. Mater.* **2013**, *12*, 836−841.

(8) Chemin, A.; Levine, I.; Rusu, M.; Vaujour, R.; Knittel, P.; Reinke, P.; Hinrichs, K.; Unold, T.; Dittrich, T.; Petit, T. Surface-mediated charge transfer of photogenerated carriers in diamond. *Small Methods* **2023**, *7*, No. e2300423.

(9) Zhang, L.; Hamers, R. J. Photocatalytic reduction of CO_2 to CO by diamond nanoparticles. *Diamond Relat. Mater.* **2017**, *78*, 24−30.

(10) Barkl, J.; Zaniewski, A. M.; Koeck, F.; Nemanich, R. J. Diamond photochemistry with visible light. *Diamond Relat. Mater.* **2019**, *96*, 195−197.

(11) Li, H.; Francisco, J. S.; Zeng, X. C. Unraveling the mechanism of selective ion transport in hydrophobic subnanometer channels. *Proc. Natl. Acad. Sci. U.S.A.* **2015**, *112*, 10851−10856.

(12) Robin, P.; Emmerich, T.; Ismail, A.; Niguès, A.; You, Y.; Nam, G.-H.; Keerthi, A.; Siria, A.; Geim, A. K.; Radha, B.; Bocquet, L. Long-term memory and synapse-like dynamics in two-dimensional nanofluidic channels. *Science* **2023**, *379*, 161−167.

(13) Abrams, D.; Trusheim, M. E.; Englund, D.; Shattuck, M. D.; Meriles, C. A. Dynamic nuclear spin polarization of liquids and gases in contact with nanostructured diamond. *Nano Lett.* **2014**, *14*, 2471−2478.

(14) Zangara, P. R.; Henshaw, J.; Pagliero, D.; Ajoy, A.; Reimer, J. A.; Pines, A.; Meriles, C. A. Two-electron-spin ratchets as a platform for microwave-free dynamic nuclear polarization of arbitrary material targets. *Nano Lett.* **2019**, *19*, 2389−2396.

(15) Lin, S.; Zhu, L.; Tang, Z.; Wang, Z. L. Spin-selected electron transfer in liquid−solid contact electrification. *Nat. Commun.* **2022**, *13*, 5230.

(16) Nemanich, R. J.; Baumann, P. K.; Benjamin, M. C.; King, S. W.; van der Weide, J.; Davis, R. F. Negative electron affinity surfaces of aluminum nitride and diamond. *Diamond Relat. Mater.* **1996**, *5*, 790−796.

(17) Nishitani, T.; Tabuchi, M.; Amano, H.; Maekawa, T.; Kuwahara, M.; Meguro, T. Photoemission lifetime of a negative electron affinity gallium nitride photocathode. *J. Vac. Sci. Technol., B: Nanotechnol. Microelectron.: Mater., Process., Meas., Phenom.* **2014**, *32*, 06F901.

(18) Yeap, W. S.; Liu, X.; Bevk, D.; Pasquarelli, A.; Lutsen, L.; Fahlman, M.; Maes, W.; Haenen, K. Functionalization of boron-doped nanocrystalline diamond with N_3 dye molecules. *ACS Appl. Mater. Interfaces* **2014**, *6*, 10322−10329.

(19) Li, S.; Bandy, J. A.; Hamers, R. J. Enhanced photocatalytic activity of diamond thin films using embedded Ag nanoparticles. *ACS Appl. Mater. Interfaces* **2018**, *10*, 5395−5403.

(20) Choudhury, S.; Kiendl, B.; Ren, J.; Gao, F.; Knittel, P.; Nebel, C.; Venerosy, A.; Girard, H.; Arnault, J.-C.; Krueger, A.; Larsson, K.; Petit, T. Combining nano-structuration with boron doping to alter sub-bandgap acceptor states in diamond materials. *J. Mater. Chem. A* **2018**, *6*, 16645−16654.

(21) Choudhury, S.; Golnak, R.; Schulz, C.; Lieutenant, K.; Tranchant, N.; Arnault, J.-C.; Pinault-Thaury, M.-A.; Jomard, F.; Knittel, P.; Petit, T. Impact of nitrogen, boron and phosphorus impurities on the electronic structure of diamond probed by X-ray spectroscopies. *C* **2021**, *7*, 28.

(22) Buchner, F.; Kirschbaum, T.; Venerosy, A.; Girard, H.; Arnault, J.-C.; Kiendl, B.; Krueger, A.; Larsson, K.; Bande, A.; Petit, T.; et al. Early dynamics of the emission of solvated electrons from nanodiamonds in water. *Nanoscale* **2022**, *14*, 17188−17195.

(23) Sun, T.; Koeck, F. A. M.; Zhu, C.; Nemanich, R. J. Combined visible light photoemission and low temperature thermionic emission from nitrogen doped diamond films. *Appl. Phys. Lett.* **2011**, *99*, 202101.

(24) Radtke, M.; Bernardi, E.; Slablab, A.; Nelz, R.; Neu, E. Nanoscale sensing based on nitrogen vacancy centers in single crystal diamond and nanodiamonds: achievements and challenges. *Nano Futures* **2019**, *3*, 042004.

(25) Casola, F.; van der Sar, T.; Yacoby, A. Probing condensed matter physics with magnetometry based on nitrogen-vacancy centres in diamond. *Nat. Rev. Mater.* **2018**, *3*, 17088.

(26) Barry, J. F.; Schloss, J. M.; Bauch, E.; Turner, M. J.; Hart, C. A.; Pham, L. M.; Walsworth, R. L. Sensitivity optimization for NV-diamond magnetometry. *Rev. Mod. Phys.* **2020**, *92*, 015004.

(27) Aslam, N.; Waldherr, G.; Neumann, P.; Jelezko, F.; Wrachtrup, J. Photo-induced ionization dynamics of the nitrogen vacancy defect in diamond investigated by single-shot charge state detection. *New J. Phys.* **2013**, *15*, 013064.

(28) Lozovoi, A.; Jayakumar, H.; Daw, D.; Vizkelethy, G.; Bielejec, E.; Doherty, M. W.; Flick, J.; Meriles, C. A. Optical activation and detection of charge transport between individual colour centres in diamond. *Nat. Electron.* **2021**, *4*, 717−724.

(29) Jayakumar, H.; Henshaw, J.; Dhomkar, S.; Pagliero, D.; Laraoui, A.; Manson, N. B.; Albu, R.; Doherty, M. W.; Meriles, C. A. Optical patterning of trapped charge in nitrogen-doped diamond. *Nat. Commun.* **2016**, *7*, 12660.

(30) Pezzagna, S.; Naydenov, B.; Jelezko, F.; Wrachtrup, J.; Meijer, J. Creation efficiency of nitrogen-vacancy centres in diamond. *New J. Phys.* **2010**, *12*, 065017.

(31) Maier, F.; Ristein, J.; Ley, L. Electron affinity of plasma-hydrogenated and chemically oxidized diamond (100) surfaces. *Phys. Rev. B: Condens. Matter Mater. Phys.* **2001**, *64*, 165411.

(32) Salvadori, M.; Araújo, W.; Teixeira, F.; Cattani, M.; Pasquarelli, A.; Oks, E.; Brown, I. Termination of diamond surfaces with hydrogen, oxygen and fluorine using a small, simple plasma gun. *Diamond Relat. Mater.* **2010**, *19*, 324−328.

(33) Cui, S.; Hu, E. L. Increased negatively charged nitrogen-vacancy centers in fluorinated diamond. *Appl. Phys. Lett.* **2013**, *103*, 051603.

(34) Dhomkar, S.; Jayakumar, H.; Zangara, P. R.; Meriles, C. A. Charge dynamics in near-surface, variable-density ensembles of nitrogen-vacancy centers in diamond. *Nano Lett.* **2018**, *18*, 4046−4052.

(35) Giri, R.; Jensen, R. H.; Khurana, D.; Bocquel, J.; Radko, I. P.; Lang, J.; Osterkamp, C.; Jelezko, F.; Berg-Sørensen, K.; Andersen, U. L.; Huck, A. Charge stability and charge-state-based spin readout of shallow Nitrogen-Vacancy centers in diamond. *ACS Appl. Electron. Mater.* **2023**, *5*, 6603−6610.

(36) Hauf, M. V.; Grotz, B.; Naydenov, B.; Dankerl, M.; Pezzagna, S.; Meijer, J.; Jelezko, F.; Wrachtrup, J.; Stutzmann, M.; Reinhard, F.; Garrido, J. A. Chemical control of the charge state of nitrogen-vacancy centers in diamond. *Phys. Rev. B: Condens. Matter Mater. Phys.* **2011**, *83*, 081304 R.

(37) Harrison, J.; Sellars, M. J.; Manson, N. B. Optical spin polarisation of the N-V centre in diamond. *J. Lumin.* **2004**, *107*, 245−248.

https://doi.org/10.1021/acsami.4c06298
ACS Appl. Mater. Interfaces 2024, 16, 37226−37233

(38) Jelezko, F.; Gaebel, T.; Popa, I.; Gruber, A.; Wrachtrup, J. Observation of coherent oscillations in a single electron spin. *Phys. Rev. Lett.* **2004**, *92*, 076401.
(39) Doherty, M. W.; Manson, N. B.; Delaney, P.; Hollenberg, L. C. L. The negatively charged nitrogen-vacancy centre in diamond: the electronic solution. *New J. Phys.* **2011**, *13*, 025019.
(40) Tetienne, J.-P.; de Gille, R. W.; Broadway, D. A.; Teraji, T.; Lillie, S. E.; McCoey, J. M.; Dontschuk, N.; Hall, L. T.; Stacey, A.; Simpson, D. A.; Hollenberg, L. C. L. Spin properties of dense near-surface ensembles of nitrogen-vacancy centers in diamond. *Phys. Rev. B* **2018**, *97*, 085402.
(41) Kim, M.; Mamin, H. J.; Sherwood, M. H.; Ohno, K.; Awschalom, D. D.; Rugar, D. Decoherence of near-surface nitrogen-vacancy centers due to electric field noise. *Phys. Rev. Lett.* **2015**, *115*, 087602.
(42) Jamonneau, P.; Lesik, M.; Tetienne, J. P.; Alvizu, I.; Mayer, L.; Dréau, A.; Kosen, S.; Roch, J.-F.; Pezzagna, S.; Meijer, J.; Teraji, T.; Kubo, Y.; Bertet, P.; Maze, J. R.; Jacques, V. Competition between electric field and magnetic field noise in the decoherence of a single spin in diamond. *Phys. Rev. B* **2016**, *93*, 024305.
(43) Myers, B. A.; Ariyaratne, A.; Jayich, A. B. Double-quantum spin-relaxation limits to coherence of near-surface nitrogen-vacancy centers. *Phys. Rev. Lett.* **2017**, *118*, 197201.
(44) Sangtawesin, S.; Dwyer, B. L.; Srinivasan, S.; Allred, J. J.; Rodgers, L. V. H.; De Greve, K.; Stacey, A.; Dontschuk, N.; O'Donnell, K. M.; Hu, D.; Evans, D. A.; Jaye, C.; Fischer, D. A.; Markham, M. L.; Twitchen, D. J.; Park, H.; Lukin, M. D.; de Leon, N. P. Origins of diamond surface noise probed by correlating single-spin measurements with surface spectroscopy. *Phys. Rev. X* **2019**, *9*, 031052.
(45) Dwyer, B. L.; Rodgers, L. V. H.; Urbach, E. K.; Bluvstein, D.; Sangtawesin, S.; Zhou, H.; Nassab, Y.; Fitzpatrick, M.; Yuan, Z.; De Greve, K.; Peterson, E. L.; Knowles, H.; Sumarac, T.; Chou, J.-P.; Gali, A.; Dobrovitski, V. V.; Lukin, M. D.; de Leon, N. P. Probing spin dynamics on diamond surfaces using a single quantum sensor. *PRX Quantum* **2022**, *3*, 040328.
(46) Laraoui, A.; Hodges, J. S.; Meriles, C. A. Nitrogen-Vacancy-assisted magnetometry of paramagnetic centers in an individual diamond nanocrystal. *Nano Lett.* **2012**, *12*, 3477−3482.
(47) Lozovoi, A.; Jayakumar, H.; Daw, D.; Lakra, A.; Meriles, C. A. Probing metastable space-charge potentials in a wide bandgap semiconductor. *Phys. Rev. Lett.* **2020**, *125*, 256602.
(48) Gao, Y.-F.; Lai, J.-M.; Sun, Y.-J.; Liu, X.-L.; Lin, C.-N.; Tan, P.-H.; Shan, C.-X.; Zhang, J. Charge state manipulation of NV centers in diamond under phonon-assisted anti-Stokes excitation of NV^0. *ACS Photonics* **2022**, *9*, 1605−1613.
(49) Bourgeois, E.; Londero, E.; Buczak, K.; Hruby, J.; Gulka, M.; Balasubramaniam, Y.; Wachter, G.; Stursa, J.; Dobes, K.; Aumayr, F.; Trupke, M.; Gali, A.; Nesladek, M. Enhanced photoelectric detection of NV magnetic resonances in diamond under dual-beam excitation. *Phys. Rev. B* **2017**, *95*, 041402 R.
(50) Gajdoš, M.; Hummer, K.; Kresse, G.; Furthmüller, J.; Bechstedt, F. Linear optical properties in the projector-augmented wave methodology. *Phys. Rev. B: Condens. Matter Mater. Phys.* **2006**, *73*, 045112.
(51) Garcia-Arellano, G.; López-Morales, G. I.; Manson, N. B.; Flick, J.; Wood, A. A.; Meriles, C. A. Photo-induced charge state dynamics of the neutral and negatively charged silicon vacancy centers in room-temperature diamond. *Adv. Sci.* **2024**, *11*, 2308814.
(52) Stacey, A.; Dontschuk, N.; Chou, J.-P.; Broadway, D. A.; Schenk, A. K.; Sear, M. J.; Tetienne, J.-P.; Hoffman, A.; Prawer, S.; Pakes, C. I.; Tadich, A.; de Leon, N. P.; Gali, A.; Hollenberg, L. C. L. Evidence for primal sp2 defects at the diamond surface: candidates for electron trapping and noise sources. *Adv. Mater. Interfaces* **2019**, *6*, 1801449.
(53) Broadway, D. A.; Dontschuk, N.; Tsai, A.; Lillie, S. E.; Lew, C. T.-K.; McCallum, J. C.; Johnson, B. C.; Doherty, M. W.; Stacey, A.; Hollenberg, L. C. L.; Tetienne, J.-P. Spatial mapping of band bending in semiconductor devices using in situ quantum sensors. *Nat. Electron.* **2018**, *1*, 502−507.
(54) Bourgeois, E.; Jarmola, A.; Siyushev, P.; Gulka, M.; Hruby, J.; Jelezko, F.; Budker, D.; Nesladek, M. Photoelectric detection of electron spin resonance of nitrogen-vacancy centres in diamond. *Nat. Commun.* **2015**, *6*, 8577.
(55) Siyushev, P.; Nesladek, M.; Bourgeois, E.; Gulka, M.; Hruby, J.; Yamamoto, T.; Trupke, M.; Teraji, T.; Isoya, J.; Jelezko, F. Photoelectrical imaging and coherent spin-state readout of single nitrogen-vacancy centers in diamond. *Science* **2019**, *363*, 728−731.
(56) Lühmann, T.; John, R.; Wunderlich, R.; Meijer, J.; Pezzagna, S. Coulomb-driven single defect engineering for scalable qubits and spin sensors in diamond. *Nat. Commun.* **2019**, *10*, 4956.
(57) Radha, B.; Esfandiar, A.; Wang, F. C.; Rooney, A. P.; Gopinadhan, K.; Keerthi, A.; Mishchenko, A.; Janardanan, A.; Blake, P.; Fumagalli, L.; Lozada-Hidalgo, M.; Garaj, S.; Haigh, S. J.; Grigorieva, I. V.; Wu, H. A.; Geim, A. K. Molecular transport through capillaries made with atomic-scale precision. *Nature* **2016**, *538*, 222−225.
(58) Staudacher, T. M.; Raatz, N.; Pezzagna, S.; Meijer, J.; Reinhard, F.; Meriles, C. A.; Wrachtrup, J. Probing molecular dynamics at the nanoscale via an individual paramagnetic centre. *Nat. Commun.* **2015**, *6*, 8527.
(59) Zhang, Q.; Guo, Y.; Ji, W.; Wang, M.; Yin, J.; Kong, F.; Lin, Y.; Yin, C.; Shi, F.; Wang, Y.; Du, J. High-fidelity single-shot readout of single electron spin in diamond with spin-to-charge conversion. *Nat. Commun.* **2021**, *12*, 1529.
(60) Irber, D. M.; Poggiali, F.; Kong, F.; Kieschnick, M.; Lühmann, T.; Kwiatkowski, D.; Meijer, J.; Du, J.; Shi, F.; Reinhard, F. Robust all-optical single-shot readout of nitrogen- vacancy centers in diamond. *Nat. Commun.* **2021**, *12*, 532.
(61) Doherty, M. W.; Meriles, C. A.; Alkauskas, A.; Fedder, H.; Sellars, M. J.; Manson, N. B. Towards a Room-Temperature Spin Quantum Bus in Diamond via Electron Photoionization, Transport, and Capture. *Phys. Rev. X* **2016**, *6*, 041035.
(62) Laraoui, A.; Meriles, C. A. Approach to dark spin cooling in a diamond nanocrystal. *ACS Nano* **2013**, *7*, 3403−3410.
(63) Navon, G.; Song, Y.-Q.; Rõõm, T.; Appelt, S.; Taylor, R. E.; Pines, A. Enhancement of solution NMR and MRI with laser-polarized xenon. *Science* **1996**, *271*, 1848−1851.
(64) Ziegler, F.; Ziegler, M. D.; Biersack, J. P. SRIM − The stopping and range of ions in matter (2010). *Nucl. Instrum. Methods Phys. Res., Sect. B* **2010**, *268*, 1818−1823.
(65) Appel, P.; Neu, E.; Ganzhorn, M.; Barfuss, A.; Batzer, M.; Gratz, M.; Tschöpe, A.; Maletinsky, P. Fabrication of all diamond scanning probes for nanoscale magnetometry. *Rev. Sci. Instrum.* **2016**, *87*, 063703.
(66) Kresse, G.; Joubert, D. From ultrasoft pseudopotentials to the projector augmented-wave method. *Phys. Rev. B: Condens. Matter Mater. Phys.* **1999**, *59*, 1758−1775.
(67) Perdew, J. P.; Burke, K.; Ernzerhof, M. Generalized gradient approximation made simple. *Phys. Rev. Lett.* **1996**, *77*, 3865−3868.
(68) Heyd, J.; Scuseria, G. E.; Ernzerhof, M. Hybrid functionals based on a screened Coulomb potential. *J. Chem. Phys.* **2003**, *118*, 8207−8215.
(69) Chou, J.; Bodrog, Z.; Gali, A. First-principles study of charge diffusion between proximate solid-state qubits and its implications on sensor applications. *Phys. Rev. Lett.* **2018**, *120*, 136401.
(70) Deák, P.; Aradi, B.; Kaviani, M.; Frauenheim, T.; Gali, A. Formation of NV centers in diamond: A theoretical study based on calculated transitions and migration of nitrogen and vacancy related defects. *Phys. Rev. B: Condens. Matter Mater. Phys.* **2014**, *89*, 075203.

https://doi.org/10.1021/acsami.4c06298
ACS Appl. Mater. Interfaces 2024, 16, 37226−37233